Journal of Power Sources 180 (2008) 773–783

Contents lists available at ScienceDirect

Journal of Power Sources

journal homepage: www.elsevier.com/locate/jpowsour

# Passive control of liquid water storage and distribution in a PEFC through flow-field design

A. Turhan, K. Heller, J.S. Brenizer, M.M. Mench*

*Fuel Cell Dynamics and Diagnostics Laboratory, Radiation Science and Engineering Center, Department of Mechanical and Nuclear Engineering, The Pennsylvania State University, University Park, PA 16802, United States*

ARTICLE INFO

*Article history:*
Received 9 January 2008
Received in revised form 8 February 2008
Accepted 11 February 2008
Available online 10 March 2008

*Keywords:*
Flooding
Polymer electrolyte fuel cell
Flow-field
Neutron imaging
Water storage
Residual water

ABSTRACT

Liquid water stored in the diffusion media (DM) in a polymer electrolyte fuel cell (PEFC) can dramatically impact steady and transient performance, degradation, and heat transfer. In this study, seven different flow-field designs, with landing-to-channel (L:C) ratio from 1:3 to 2:1, were investigated at dry and fully humidified conditions, using neutron imaging. The results revealed the impact of flow-field geometry on stored liquid overhead is significant. In some cases, the stored water content in the cell can be nearly double that of another design, despite similar performances at low to medium current density. In general, a smaller L:C ratio reduces flooding losses and minimizes the stored water content. Additionally, the channel–DM interface plays a key role. For the same L:C ratio, a reduced number of channel–DM interfaces was shown to reduce flooding and stored liquid water content at steady state. This also suggests that using proper flow-field design can decrease the parasitic power consumption and the stored water content in the cell without any sacrifice from the cell performance. For dryer operating conditions, however, membrane dehydration becomes a dominant effect and a high landing-to-channel ratio flow-field is higher performing.



## 1. Introduction

A well-hydrated polymer electrolyte is critical for suitable ionic conductivity in a polymer electrolyte fuel cell (PEFC) [1–5]. On the other hand, the existence of excess liquid water in the fuel cell catalyst layer, diffusion media (DM) and flow channels can severely limit performance. In literature, there are many modeling [e.g. 3, 6–17] and experimental [e.g. 18–30] studies regarding the effect of water management on cell performance with respect to short-term, recoverable flooding performance loss. Furthermore, the liquid water stored in the fuel cell during regular operation can have a strong influence on catalyst and carbon support degradation, ionic contamination of the membrane electrode assembly (MEA), and damage occurring during freeze/thaw cycling [31–35].

Although there are various studies reported in the literature on flow-field design of PEFCs [36–50], the effect of flow-field configuration, specifically on water storage, is not yet thoroughly understood. Wood et al. [40] studied the effects of interdigitated flow-field design. Their results indicated that the dead-ended flow channels in interdigitated flow-field design could operate with more liquid water in the anode compartment without causing severe transport losses. In an other study, Chen et al. [41] performed modeling simulations with variable channel heights and concluded that larger channel height enables higher power density, although this would reduce stack power density. Kumar and Reddy [42] also studied the effect of flow-field design on cell performance by modeling the hydrogen consumption rate at the anode. Their results indicated that more efficient hydrogen consumption resulted from hemispherical and triangular channel cross-sections compared to rectangular cross-section, due to decreased landing width. In another study, Liu et al. [44] performed a numerical study on the effects of tapered flow-field design, where channel depth is reduced along the stream wise direction. They defined $R_{ch}$ as the ratio of the outlet channel depth to the inlet channel depth. At low current, $R_{ch}$ has an insignificant effect on the performance. At high current operation, however, they found that smaller $R_{ch}$ yields higher limiting current values. Their results also showed a lower liquid saturation in the DM at the small $R_{ch}$ values. Knights and Wilkinson [45] also investigated the tapered design by varying the channel width from inlet to outlet. They showed that this flow-field configuration also improves fuel cell performance in terms of increased limiting current density.

Neutron imaging is a powerful tool to investigate the water accumulation and storage inside a fuel cell flow channels and diffusion media. Recently, several studies were conducted on water manage-

* Corresponding author. Tel.: +1 814 865 0060; fax: +1 814 863 4848.
*E-mail address:* mmm124@psu.edu (M.M. Mench).

0378-7753/$ – see front matter © 2008 Elsevier B.V. All rights reserved.
doi:10.1016/j.jpowsour.2008.02.028

ment phenomena in fuel cells using this technique [51–60]. Kramer et al. [51] investigated the liquid water accumulation in two different flow-field geometries; a ten-channel serpentine design and a fifty-channel interdigitated design. Both designs have the same channel and landing width, depth and landing-to-channel (L:C) ratio. They found more liquid formation in the interdigitated case, mostly near the dead ends. Liquid in the channels was removed more efficiently by the serpentine design. Also for this design, liquid was found to be the highest at the exit region. In part B of their work [52], they performed neutron imaging tests on two different flow-field material; gold-coated aluminum and thin graphite. For both cases, dependence of the water accumulation to the temperature was tested by varying the position of the heater cartridges, and liquid accumulation was found to be highly sensitive to the temperature profile in the cell. The gold-coated aluminum flow field avoids significant liquid cluster formation better than the graphite and therefore reduces the liquid amount in the flow channels since it is more hydrophilic. The liquid variation in the MEA structure was investigated with neutron imaging by Ludlow et al. [54]. They performed experiments with humidified gases, and at the end of the operation, they took a reference image. Then, the cell was dried for 20 min and images of the dry state were taken. The results showed liquid was removed first from the flow channels and then from the DM and membrane. In an other study, Chen et al. [55] used a specially designed cell to differentiate the anode side from the cathode in neutron images. The cathode channels were shifted by a channel width, hence anode and cathode flow field did not overlap. They divided the active area into four regions and calculated water thicknesses for each region. Their results indicated significant liquid accumulation in the anode DM that decreased with increasing current. It is also possible to detect the transient behavior of water accumulation in the fuel cell with neutron imaging. Hickner et al. [56] investigated the transient water storage in the fuel cell together with the local heating effects on water distribution. They observed that at 80 °C cell temperature, with a step change in current from 0 to 1500 mA cm$^{-2}$, there was a delay of ~110 s in liquid water accumulation after applying the current and it took ~200 s to reach a pseudo-steady-state condition for the fuel cell used. They also suggested once liquid water formed in the DM, it is very hard to remove it by advection. Their results also showed that at 40 °C there is a monotonic increase in stored liquid water with increasing current, whereas at 80 °C, liquid water in the cell first increases up to a critical current value and further increase in the current reduces the stored water amount. This finding is also consistent with Turhan et al. [58]. Kowal et al. [59] also investigated the transient behavior of liquid water accumulation by applying a 0.1-A cm$^{-2}$ step change from 0.2 to 0.7 A cm$^{-2}$ and obtaining continuous stream of neutron images. Allowing 20 s between each step change, it was found that the slope of water mass accumulated in the cell increases at each step change, consistent with Faraday's law.

Despite the various published experimental and modeling research on the characterization of the diffusion media and flow-field effect, there is limited understanding of the combined role of the land/channel and DM interface on the liquid water storage and distribution, and most multiphase flow models do not consider this important interaction due to the complexity of including multiphase flow in the open channel. The motivation of this study was to understand the implication of L:C ratio and channel–DM interface on the liquid water content stored in the diffusion media and flow channels during steady-state operation. Neutron imaging at the Penn State Breazeale Nuclear Reactor Fuel Cell Imaging Laboratory was used to quantify liquid water content and distribution in 50 cm$^2$ fuel cells with L:C ratios from 1:3 to 2:1.

## 2. Experimental

Neutron imaging is a non-intrusive in situ diagnostic which can be used on an unmodified fuel cell with accurate flow field and thermal boundary conditions. The neutron imaging experiments in this study were conducted at the Penn State Breazeale Nuclear Reactor (PSBR) and Radiation Science and Engineering Center (RSEC) Fuel Cell Imaging Laboratory. For image processing, storage and water quantification analysis, specialized in-house hardware was developed [57]. The temporal and spatial resolution for radioscopy shown here is approximately 30 frames s$^{-1}$ and 129 μm per pixel in the 50 cm$^2$ active area. Current technology of RSEC allows full sized stack cell imaging with greatly enhanced resolution. Further details about the nuclear facilities and image processing hardware are available in Turhan et al. [58].

An integrated Neutron Beam Laboratory Fuel Cell Test Station (NBLTS) is used to control and monitor the fuel cell operating parameters, and is isolated from the neutron beam source. The station can accommodate various sized fuel cells (up to 25.4 cm$^2$ in a single frame and larger areas by motion on an installed hydraulic platform with up to 1000 A current output) for neutron imaging processes, at frozen to normal operating temperatures.

A video capturing software program, Streampix, collects and records the fully digital video signal produced by the CCD camera system without data compression for analysis purposes. A total of 60 images at five frames per second for 12 s were taken for each steady-state fuel cell condition and averaged to reduce instrument noise and pixel variance. False colorization of liquid water to correspond to the measured liquid water thickness in the fuel cell was also used to improve qualitative analysis. Further details on image processing and calibrated water quantification techniques can be found in Turhan et al. [58].

It should be noted that the anode and cathode side inlet and exit manifolds, where large water slugs can periodically accumulate and flush, were not included in the water quantification process to reduce error and increase water thickness sensitivity, which is 12.7 μm on the system used for the tests in this paper (a new system at PSU reaches approximately 4 μm sensitivity). Additionally, the portion of the flow field where the heaters are placed was also removed from image analysis area in order to eliminate the heater artifact caused by thermal expansion. The total area removed from processing amounts to ~10% of the cell area, so that the total water in the 50 cm$^2$ cell should be slightly greater than the quantified amount. The quantification of liquid water within the cell is comprised of line-averages of water through the entire fuel cell assembly (i.e., gas flow channels, MEA, and gas diffusion media). Therefore, it is not possible to directly distinguish between anode and cathode water content with the aligned cells used, without neutron tomography. Channel droplet location can be inferred from the direction of motion on video, however. It is also possible to determine the amount of water under the landings and in, or under the flow channels,

**Table 1**
Experimental test matrix

| Cell configuration landing-channel | Current density (A cm$^{-2}$) | Inlet relative humidity (%) |
|---|---|---|
| 0.5 × 0.5 | 0 → 1.5 | 50/100 |
| 0.5 × 1.5 | 0 → 1.5 | 50/100 |
| 1.0 × 0.75 | 0 → 1.5 | 50/100 |
| 1.0 × 1.0 | 0 → 1.5 | 50/100 |
| 1.0 × 1.5 | 0 → 1.5 | 50/100 |
| 2.0 × 1.0 | 0 → 1.5 | 50/100 |
| 2.0 × 2.0 | 0 → 1.5 | 50/100 |

All tests were performed at 80 °C, 150 kPa, anode/cathode stoichiometry of 2/2.

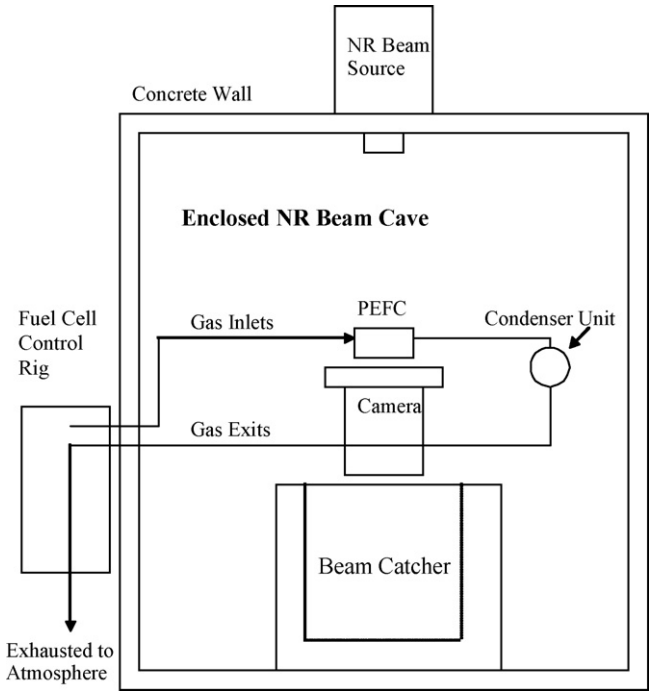


**Fig. 1.** Test stand for neutron imaging experiments.

using a digital masking technique with software developed at PSU.

A 50-cm$^2$ active area fuel cell with seven different flow-field patterns was used for testing. The landing and channel sizes were varied between 0.5 and 2.0 mm. The related properties of each configuration are shown in Table 1 along with the detailed test matrix. A 25-μm thick, 0.4/0.4 mg cm$^{-2}$ Pt loading Gore 5510 MEA and a 210-μm thick, 70% porosity, Johnson–Matthey diffusion media with MPL were used in all configurations. In all configurations, fully humidified inlet conditions at the cell temperature were maintained with 150 kPa (7.35 psig) cell pressure and anode/cathode stoichiometries of 2/2, and a counter-flow serpentine/parallel combination arrangement. Ultra-high purity hydrogen and air were used as the fuel and oxidant, respectively. Fig. 1 is a schematic of the test system. All flow meters and humidifiers used were precisely and regularly calibrated.

## 3. Results and discussion

### 3.1. Fully humidified testing

#### 3.1.1. Landing/channel ratio effect

The effect of L:C ratio was investigated through seven different flow designs with different landing and channel widths. The flow-field dimensions, flow channel gas velocities and measured liquid water amounts at each current condition are given in Table 2. In four of those designs, the L:C ratio is different than one, whereas the remaining three flow fields have a L:C ratio of one but with different number of channel–DM interfaces. Additionally, some configurations have the same channel width and some have the same landing width. The results are presented in three categories for clarity: (1) different L:C ratios with the same landing width (channel size effect), (2) different L:C ratios with same channel width (landing size effect), and (3) different L:C ratios with different L:C widths.

*3.1.1.1. Channel size effect.* In Fig. 2a and b, neutron images of cell configurations 1.0 × 1.5 and 1.0 × 0.75 (L:C) are shown. All the images are also available in color at http://www.mne.psu.edu/fuelcell/NR#4.html. Note that since these two configurations have the same landing width, the L:C ratio effect can be analyzed in terms of channel size.

At 0.2 A cm$^{-2}$ current density, the water content calculated for the small L:C ratio (large channel, Fig. 2a) configuration (361 mg) is almost 50% less than the large L:C ratio (small channel configuration, Fig. 2b, 515 mg). A greater portion of the excess water in the small channel case is found to be under the landings (281–151 mg) compared to in, or under the channels (234–210 mg). In Fig. 3a and b, cell configurations 0.5 × 1.5 and 0.5 × 0.5 are shown. The total stored water in 0.5 × 0.5 configuration at 0.8 A cm$^{-2}$ is 468 mg, ~66% greater than 0.5 × 1.5 case which is a similar result.

It is possible that between a small and large channel case, the difference in the measured liquid amount is due to the different channel areas and does not reveal the true L:C ratio effect. In order to clarify the effect of L:C ratio, the calculated water mass values from the neutron images were normalized according to the corresponding geometry and compared. In this calculation, the total

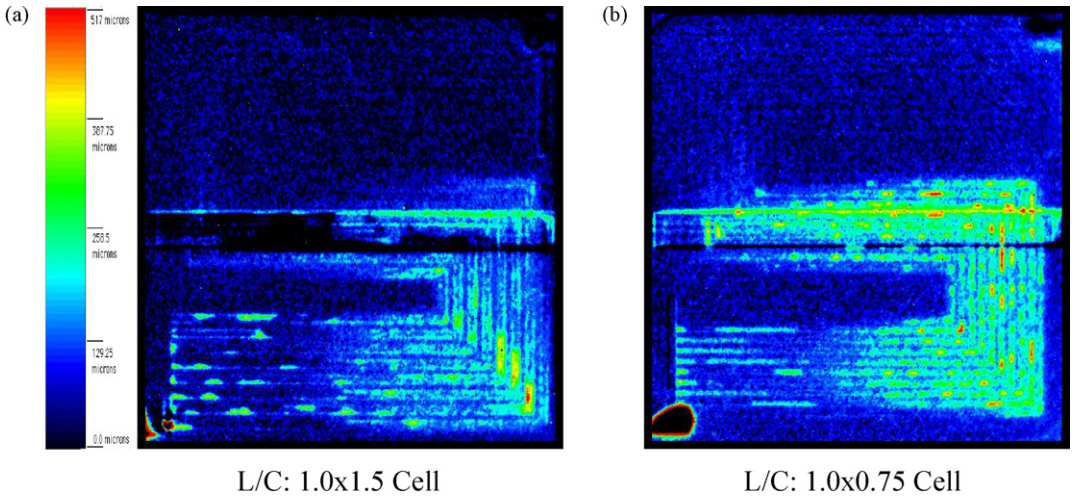


**Fig. 2.** Neutron images of (a) 1.0 × 1.5 and (b) 1.0 × 0.75 cell configurations at 10 A, 100% RH, 150 kPa (7.35 psig) operating conditions. (a) Total liquid water mass = 361 mg, land DM liquid water mass = 151 mg, and channel liquid water mass = 210 mg. (b) Total liquid water mass = 515 mg, land DM liquid water mass = 281 mg, and channel liquid water mass = 234 mg.

**Table 2**
Calculated steady-state water mass values under the landings (L) and in, or under the channels (CH) are shown together with the flow velocities

| Current density ($A\,cm^{-2}$) | Cell configuration | | | | | | | | | | | |
|---|---|---|---|---|---|---|---|---|---|---|---|---|
| | L:C 0.5 × 0.5 | | | | | | L:C 0.5 × 1.5 | | | | | |
| | 50 RH | | 100 RH | | Cathode velocity ($m\,s^{-1}$) | Anode velocity ($m\,s^{-1}$) | 50 RH | | 100 RH | | Cathode velocity ($m\,s^{-1}$) | Anode velocity ($m\,s^{-1}$) |
| | CH (mg) | L (mg) | CH (mg) | L (mg) | | | CH (mg) | L (mg) | CH (mg) | L (mg) | | |
| 0.2 | 110 | 152 | 209 | 231 | 1.36 | 1.04 | 172 | 75 | 254 | 99 | 0.90 | 0.69 |
| 0.4 | 113 | 150 | 279 | 292 | 2.71 | 2.08 | 81 | 43 | 323 | 119 | 1.81 | 1.39 |
| 0.6 | 91 | 125 | 242 | 254 | 4.07 | 3.13 | 69 | 38 | 253 | 109 | 2.71 | 2.08 |
| 0.8 | 64 | 100 | 223 | 245 | 5.43 | 4.17 | 71 | 38 | 193 | 88 | 3.62 | 2.78 |
| 1.0 | 53 | 86 | 174 | 215 | 6.79 | 5.21 | 60 | 32 | 143 | 68 | 4.52 | 3.47 |
| 1.2 | 55 | 91 | 164 | 211 | 8.14 | 6.25 | 72 | 39 | 154 | 70 | 5.43 | 4.17 |
| 1.4 | 56 | 91 | | | 9.50 | 7.29 | 85 | 44 | 124 | 60 | 6.33 | 4.86 |
| 1.5 | | | | | 10.18 | 7.81 | | | 141 | 67 | 6.79 | 5.21 |

| Current density ($A\,cm^{-2}$) | Cell configuration | | | | | | | | | | | |
|---|---|---|---|---|---|---|---|---|---|---|---|---|
| | L:C 1.0 × 1.0 | | | | | | L:C 1.0 × 1.5 | | | | | |
| | 50 RH | | 100 RH | | Cathode velocity ($m\,s^{-1}$) | Anode velocity ($m\,s^{-1}$) | 50 RH | | 100 RH | | Cathode velocity ($m\,s^{-1}$) | Anode velocity ($m\,s^{-1}$) |
| | CH (mg) | L (mg) | CH (mg) | L (mg) | | | CH (mg) | L (mg) | CH (mg) | L (mg) | | |
| 0.2 | 163 | 167 | 269 | 256 | 1.36 | 1.04 | 79 | 73 | 210 | 151 | 1.21 | 0.93 |
| 0.4 | 94 | 118 | 300 | 283 | 2.71 | 2.08 | 81 | 74 | 240 | 174 | 2.41 | 1.85 |
| 0.6 | 81 | 116 | 273 | 278 | 4.07 | 3.13 | 79 | 73 | 218 | 161 | 3.62 | 2.78 |
| 0.8 | 73 | 110 | 230 | 260 | 5.43 | 4.17 | 78 | 73 | 188 | 169 | 4.83 | 3.70 |
| 1.0 | 56 | 89 | 212 | 247 | 6.79 | 5.21 | 91 | 85 | 158 | 152 | 6.03 | 4.63 |
| 1.2 | 59 | 92 | 189 | 228 | 8.14 | 6.25 | 71 | 67 | 111 | 122 | 7.24 | 5.56 |
| 1.4 | 57 | 90 | 191 | 227 | 9.50 | 7.29 | 75 | 70 | 101 | 107 | 8.44 | 6.48 |
| 1.5 | 55 | 86 | 170 | 211 | 10.18 | 7.81 | 67 | 63 | 104 | 110 | 9.05 | 6.95 |

| Current density ($A\,cm^{-2}$) | Cell configuration | | | | | | | | | | | |
|---|---|---|---|---|---|---|---|---|---|---|---|---|
| | L:C 1.0 × 0.75 | | | | | | L:C 2.0 × 1.0 | | | | | |
| | 50 RH | | 100 RH | | Cathode velocity ($m\,s^{-1}$) | Anode velocity ($m\,s^{-1}$) | 50 RH | | 100 RH | | Cathode velocity ($m\,s^{-1}$) | Anode velocity ($m\,s^{-1}$) |
| | CH (mg) | L (mg) | CH (mg) | L (mg) | | | CH (mg) | L (mg) | CH (mg) | L (mg) | | |
| 0.2 | 85 | 126 | 234 | 281 | 1.67 | 1.28 | 95 | 204 | 268 | 363 | 2.04 | 1.56 |
| 0.4 | 86 | 127 | 270 | 301 | 3.34 | 2.56 | 76 | 170 | 307 | 428 | 4.07 | 3.13 |
| 0.6 | 94 | 140 | 412 | 403 | 5.01 | 3.85 | 79 | 182 | 271 | 394 | 6.11 | 4.69 |
| 0.8 | 89 | 133 | 322 | 354 | 6.68 | 5.13 | 88 | 195 | 190 | 354 | 8.14 | 6.25 |
| 1.0 | 98 | 145 | 247 | 306 | 8.35 | 6.41 | 90 | 200 | 174 | 333 | 10.18 | 7.81 |
| 1.2 | 92 | 136 | 205 | 284 | 10.02 | 7.69 | 81 | 179 | | | 12.21 | 9.38 |
| 1.4 | 77 | 115 | 180 | 257 | 11.69 | 8.98 | | | | | 14.25 | 10.94 |
| 1.5 | 72 | 109 | | | 12.53 | 9.62 | | | | | 15.27 | 11.72 |

| Current density ($A\,cm^{-2}$) | Cell configuration (L:C 2.0 × 2.0) | | | | | |
|---|---|---|---|---|---|---|
| | 50 RH | | 100 RH | | Cathode velocity ($m\,s^{-1}$) | Anode velocity ($m\,s^{-1}$) |
| | CH (mg) | L (mg) | CH (mg) | L (mg) | | |
| 0.2 | 77 | 92 | 190 | 177 | 1.36 | 1.04 |
| 0.4 | 80 | 95 | 227 | 200 | 2.71 | 2.08 |
| 0.6 | 80 | 95 | 142 | 187 | 4.07 | 3.13 |
| 0.8 | 75 | 90 | 126 | 172 | 5.43 | 4.17 |
| 1.0 | 75 | 89 | 100 | 140 | 6.79 | 5.21 |
| 1.2 | 67 | 81 | 90 | 118 | 8.14 | 6.25 |

channel and landing area of each design was taken as the normalization parameter and calculated water mass values were divided by these areas. It is important to note that the normalized water value was calculated by using the compressed thickness of the DM and considering all the water mass being in *only one DM*, which is the worst case scenario, since there is some liquid storage in the anode DM, as shown by Hickner et al. [56]. In Fig. 4, the normalized water contents of 0.5 × 1.5 and 0.5 × 0.5 cell configurations are shown as a function of current density. The difference in saturation can be clearly seen. For example, at 0.8 $A\,cm^{-2}$, the water amount under the landings for 0.5 × 1.5 cell is 88 mg and the landing area of this configuration is 11.8 $cm^2$. Hence, volumetric saturation level under the landings for this configuration is ~7.5 $mg\,cm^{-3}$. The 0.5 × 0.5 cell on the other hand, has 245 mg water under the landings with its landing area being 24.5 $cm^2$. Thus, the saturation level under the landings for this case is increased to ~10.5 $mg\,cm^{-3}$. The difference in the stored water per unit L:C area indicates the L:C ratio has a significant impact on the stored water content, with a higher

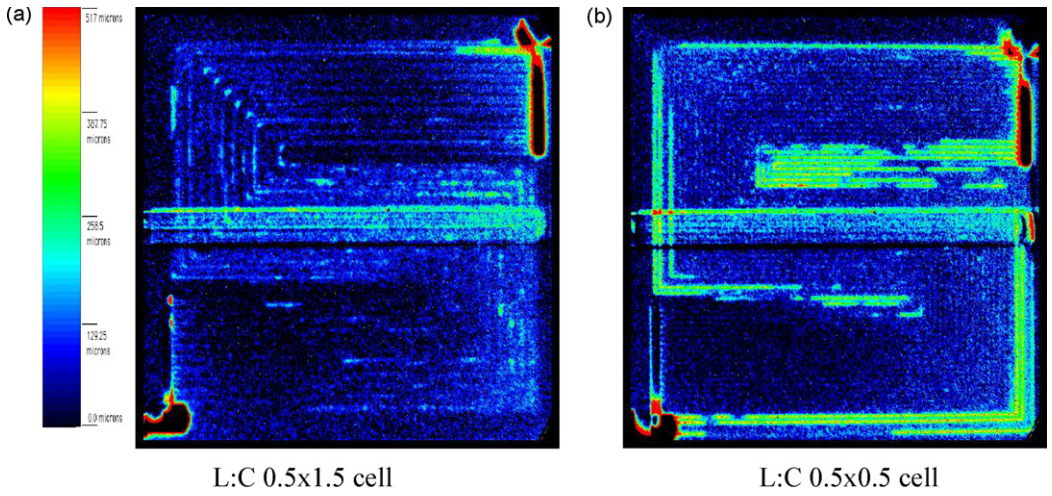


**Fig. 3.** Neutron images of (a) 0.5 × 1.5 and (b) 0.5 × 0.5 cell configurations at 40 A, 100% RH, 150 kPa (7.35 psig) operating conditions are shown. (a) Total liquid water mass = 281 mg, land DM liquid water mass = 88 mg, and channel liquid water mass = 193 mg. (b) Total liquid water mass = 468 mg, land DM liquid water mass = 245 mg, and channel liquid water mass = 223 mg.

L:C ratio increasing the stored water content. Another observation from Fig. 4 is that with increasing current, stored water content first increases and then decreases. This critical current is 20 A for both of the configurations. This behavior was also observed in the study of Hickner et al. [56] and Turhan et al. [58]. In the low current region, there is low reactant flow rate and low heat generation at the catalyst layer. In this condition, the cell temperature is maintained by the heating cartridge since the self-heating by reaction is not adequate. These effects reduce the amount of water removed from the cell by either shear force or evaporation. As the current is increased, the flow rate and heat generation in the catalyst layer also increases and more water can be removed from the cell in vapor and liquid phases. There is a critical current value and above this value, water removal from the cell overcomes the increased water production in the cell and total amount of water in the cell decreases, both due to the increased shear forces and the self-heating of the cell. It should be noted that this behavior is dependent on the thermal boundary conditions and can be different if the heating cartridges are replaced with coolant channels.

The cell performance data of 0.5 × 0.5 and 0.5 × 1.5 configurations are shown in Fig. 5. At 1.2 A $cm^{-2}$, the volumetric liquid saturations under the landings of these two configurations are 9.5 and 6.5 mg $cm^{-3}$. The kinetic and ohmic regions for each configuration are almost identical, despite very different water storage. However, the mass transfer region of the performance curves shows significant difference. For the small channel case, there is a decrease in the performance in this region due to flooding losses, not observed for the large channel configuration.

In Fig. 6, a possible liquid water accumulation scenario in the DM is illustrated that is consistent with the results shown. For the small channel configuration, water will accumulate under the lands and increase saturation at these locations, until the capillary pressure increases to a point where lateral in-plane transport of the liquid takes place. This in-plane flow will either be pushed into the channel, or unite with water being pushed laterally from an adjacent channel. If the side-by-side water pathways connect in the DM before exiting the DM through the channel, severe mass transport loss can occur. Thus, the ratio of in plane to through plane liquid permeability in the DM material should be considered as an important parameter for flooding losses. This also explains the greater flooding losses experienced for fuel cell designs with very narrow channel dimensions. For the large channel case, although there is still some liquid water in the DM, due to absence of saturated and connected DM structure, performance at high current region is much better compared to the small channel case.

*3.1.1.2. Landing size effect.* In Fig. 7a and b, neutron images of two different flow-field configurations, 2.0 × 1.0 and 1.0 × 1.0 (L:C), are

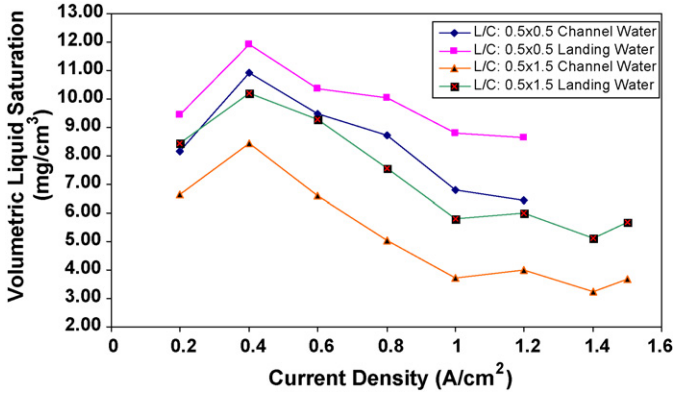


**Fig. 4.** Normalized water mass values for 0.5 × 0.5 and 0.5 × 1.5 configurations at 100% RH. Larger channels tend toward lower liquid saturation, since the DM under lands generally carry a higher liquid saturation.

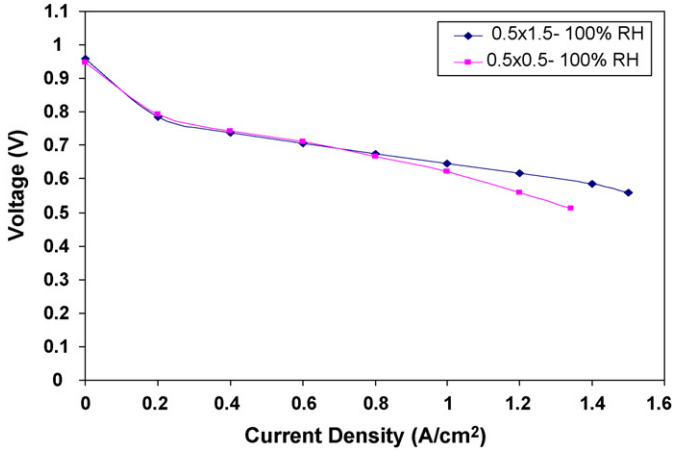


**Fig. 5.** Polarization curves for cell configurations 0.5 × 0.5 and 0.5 × 1.5. Performance loss due to flooding behavior is observed for the small channel configuration, indicating the effect of channel size on cell performance.

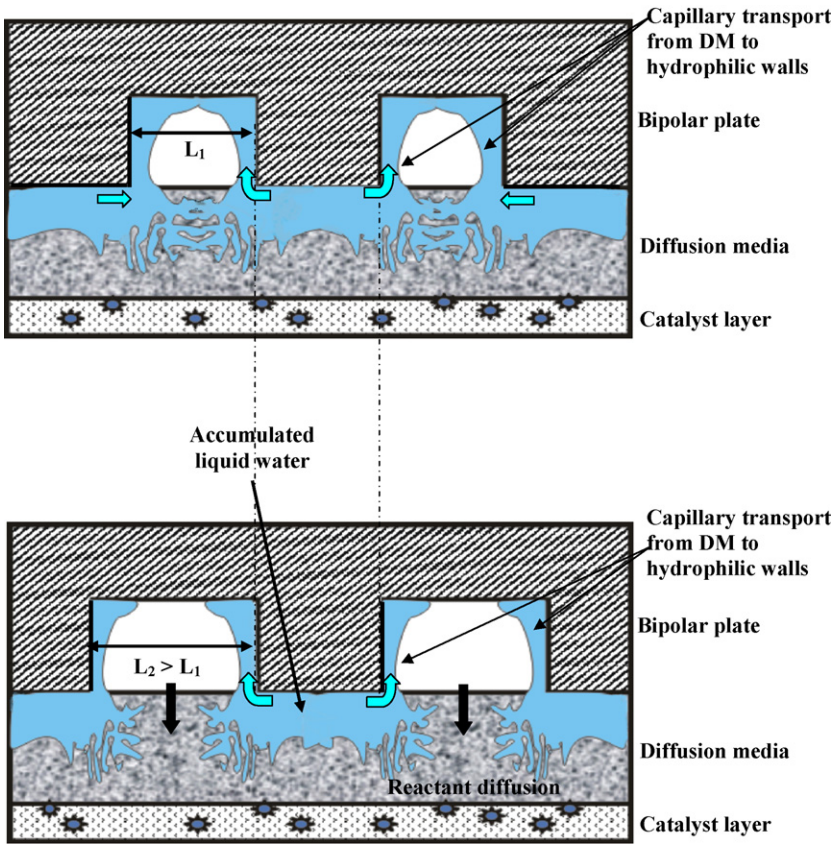


**Fig. 6.** Schematic of a possible flooding behavior for small channel and large channel configurations.

shown where L:C ratios are 2 and 1, respectively. Note that first configuration has twice the land width of the second case with the same channel size.

The calculated water mass value under the landings for $2.0 \times 1.0$ case is 428 mg, 40% greater than that in, or under the channels. This is expected for a couple of reasons: (1) thermal effects, such that condensation of water vapor on landing surfaces due to high heat removal rate, and (2) inability for water removal from these locations. The water content in both configurations at $0.4\,A\,cm^{-2}$ was compared and it is observed there is more residual water in the large landing configuration (735 mg) than small (584 mg). The volume normalized water mass values for $2.0 \times 1.0$ and $1.0 \times 1.0$ configurations are plotted in Fig. 8. The liquid saturation levels for each configuration were observed to be different, indicating there is an independent landing effect on water accumulation and storage. From the figure, it is observed that there is a higher liquid saturation for large landing case.

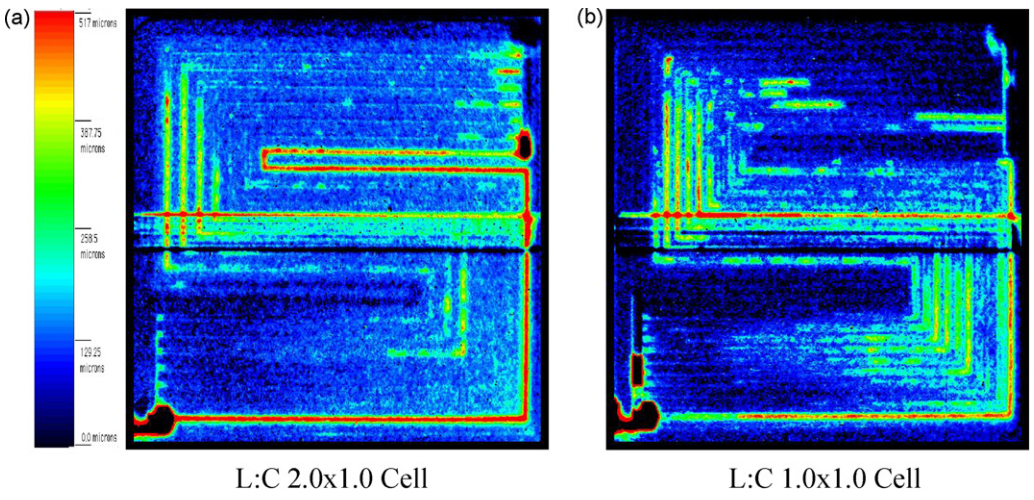


**Fig. 7.** Neutron images of (a) $2.0 \times 1.0$ and (b) $1.0 \times 1.0$ cell configurations at 20 A ($0.4\,A\,cm^{-2}$), 100% RH, 150 kPa (7.35 psig) operating conditions with the calculated water mass values. (a) Total liquid water mass = 735 mg, land DM liquid water mass = 428 mg, and channel liquid water mass = 307 mg. (b) Total liquid water mass = 583 mg, land DM liquid water mass = 283 mg, and channel liquid water mass = 300 mg.

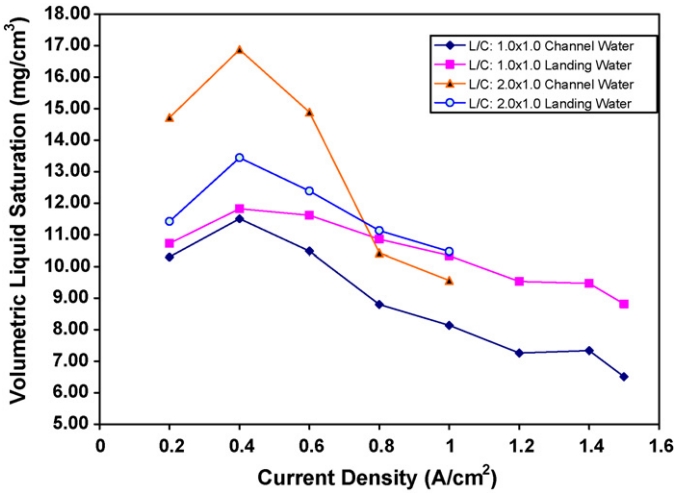


**Fig. 8.** Normalized water mass values for $2.0 \times 1.0$ and $1.0 \times 1.0$ configurations. Larger landings tend toward higher liquid saturation as current increased.

A performance comparison for each configuration was also made. As seen in Fig. 9, the performances of both cells are almost identical at low current, although the residual water contents are very different. For example, at 0.2 A $cm^{-2}$ condition, both configurations are at 0.784 V. However, in the large landing case, there is 25%

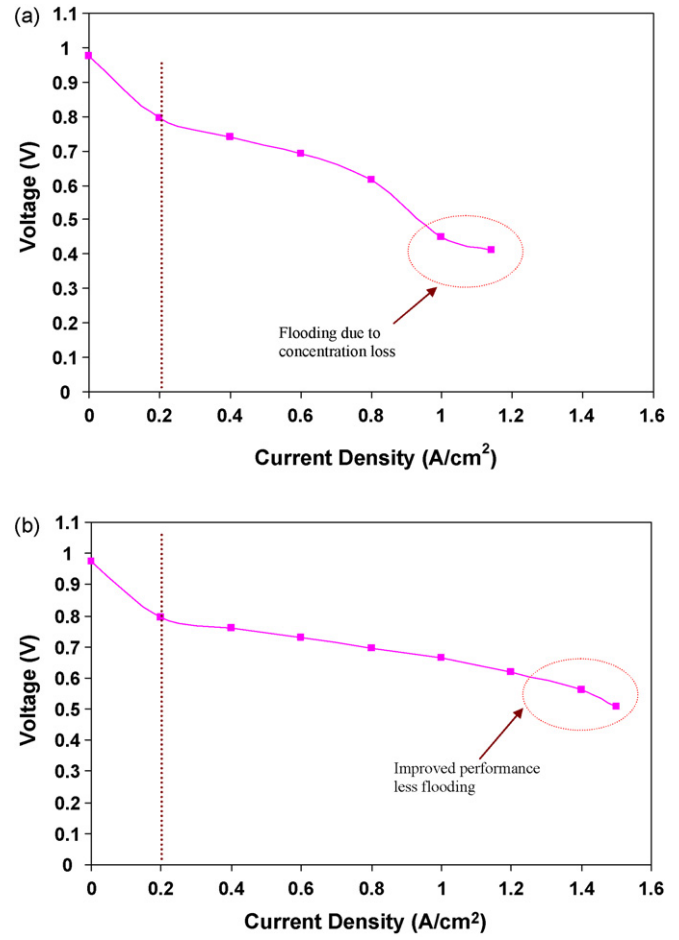


**Fig. 9.** Cell performance curves of (a) $2.0 \times 1.0$ and (b) $1.0 \times 1.0$ configurations. The water amount in $2.0 \times 1.0$ case is 25% more than $1.0 \times 1.0$ case although performances are almost identical at 10 A (0.2 A $cm^{-2}$).

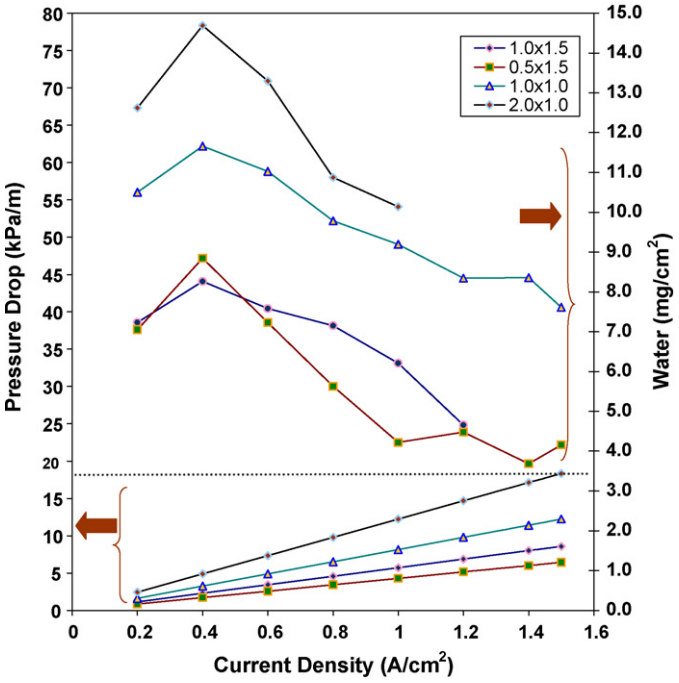


**Fig. 10.** Pressure drop and water amount is plotted at each current density condition for $1.0 \times 1.5$, $0.5 \times 1.5$, $1.0 \times 1.0$ and $2.0 \times 1.0$ cell configuration.

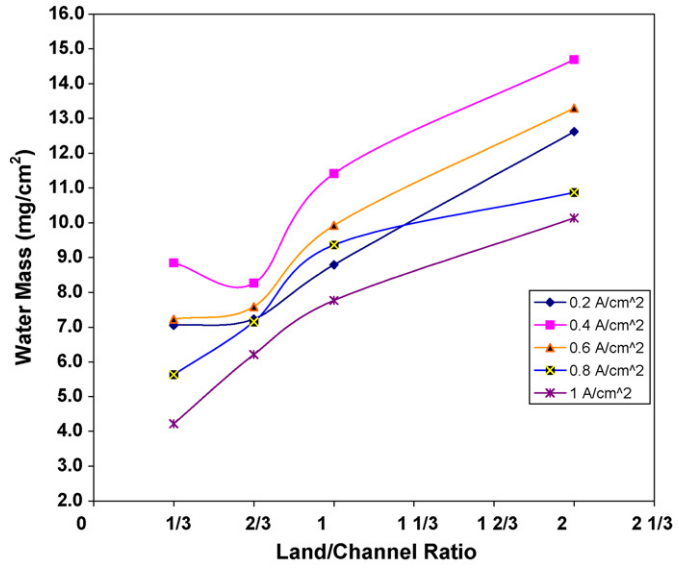


**Fig. 11.** Water mass values for configurations that have landing-to-channel ratio different than unity. In general, the larger the land/channel ratio, the greater the liquid accumulated in the cell.

more liquid water compared to small landing case (631–525 mg). Hence, it is clear that, operating current is not the only criterion determining the water accumulation in the cell. Due to different flow-field geometries, there can be vastly different residual water content in the cell even though electric power output and even efficiency are identical. This result has important implications on freeze/thaw, cold start and durability. Obviously, the least residual water overhead is most desirable. The second observation from the figure is the difference in flooding behavior between two configu-

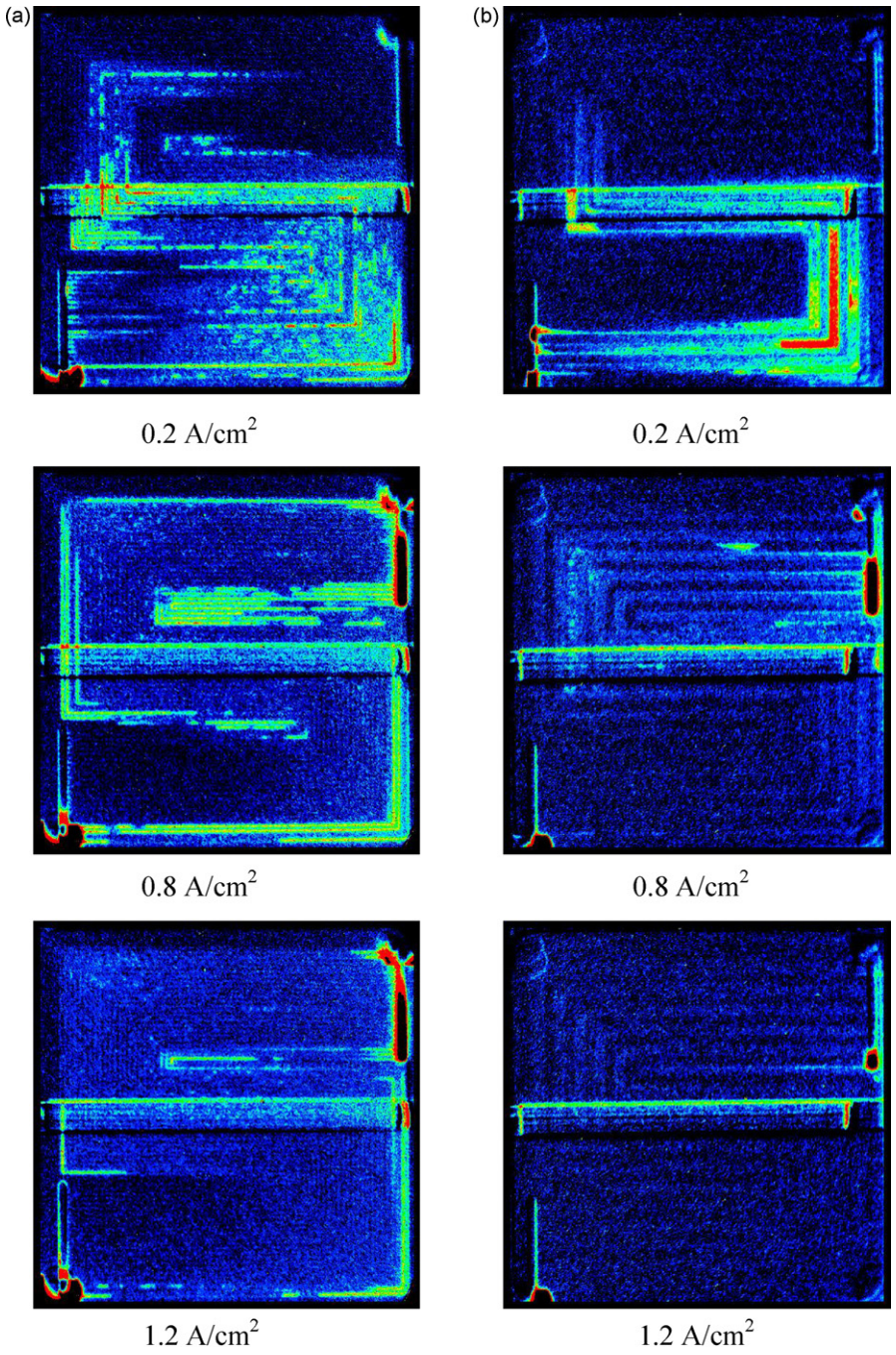


**Fig. 12.** Neutron images for (a) 0.5 × 0.5 and (b) 2.0 × 2.0 are shown. As the interface number decreases so does the stored water amount.

rations. In larger landing case, a significant performance drop due to mass transport limitation occurs, whereas for the small landing case, improved performance at high current is observed. The main reasons of losses at high current region for larger landing case are flooding due to high water accumulation, decreased mass transfer area and larger mass transfer resistance. It is also important to note that the small landing area results in higher electrical resistance and increased ohmic losses. However, for these configurations, it is seen that the improved mass transport obtained at small landing case overcomes the increased electrical resistance and yields a better cell performance. Hence, in terms of obtaining best performance while minimizing stored water, a small landing size is preferred in high humidity conditions.

For a given flow-field configuration, increasing the flow rate of the inlet gases reduces the residual water content in the cell. This is not a preferred method to remove the liquid from the cell since it requires additional power to supply the high flow rates and therefore reduces the overall efficiency. Tailoring the flow-field geometry for reduced liquid overhead is a solution to passively reduce the liquid while keeping the pressure drop at a minimum. In Fig. 10, the measured water mass and calculated cathode pressure drop values are plotted at each current density. Pressure drop is calculated by assuming steady, laminar, and fully developed single-phase flow in the channels with minor losses neglected. Conditions 1.0 × 1.0 and 2.0 × 1.0 are chosen here to describe the landing size effect. At 0.4 A cm$^{-2}$ condition, Fig. 10 shows that calculated cathode

pressure drop for the small landing configuration is ~3.3 kPa $m^{-1}$, whereas the large landing pressure drop is ~4.9 kPa $m^{-1}$. That is small landing configuration has ~33% lower channel pressure drop without liquid droplets. At the same time, the measured residual water in this configuration is ~21% lower than larger landing case (583 and 735 mg, respectively) with almost the same performance (0.747 and 0.740, respectively). The behavior is similar for the different channel configurations and this trend is observed at all the current density conditions. This suggests that, using proper flow-field design can decrease the parasitic power consumption and the stored water in the cell without any sacrifice from the cell performance.

*3.1.1.3. Land/channel ratio with mixed landing/channel width.* For high humidity conditions, increasing only the channel width tends to reduce the liquid accumulation and increasing only the landing width tends to increase the liquid stored. However, the net result of these two effects is still unclear for a case where both channel and landing widths are increased. For example, between 0.5 × 0.5 to 2.0 × 1.0 cases, the landing size is increased four times, which should increase the stored liquid, and the channel size is doubled, which should decrease the liquid amount. It is unclear which effect should dominate. The same is true between 0.5 × 0.5 and 1.0 × 1.5 cases. Therefore, to obtain a generalized understanding of the L:C ratio effect, testing of flow-field configurations with both different landing width and channel width were conducted. In Fig. 11, water mass values of 0.5 × 0.5, 2.0 × 1.0, 1.0 × 1.5 and 0.5 × 1.5 are shown. From the figure it is possible to see that for almost all of the current densities, the stored liquid in the cell increases with increasing L:C ratio. So for the 0.5 × 0.5 case, even though there are narrower channels compared to the 2.0 × 1.0 case, the small landing width dominates the liquid removal and overall there is less liquid storage in the cell. Based on a simple single-phase mass transfer calculation shown in the Appendix A, mass transfer in the 1:3 (L:C) case is 1.6 times higher than the 4:3 (L:C) case, which might be a reason for the difference in the steady water mass values. This suggests it is better to design small L:C ratios in order to decrease the residual water content in the cell. Specifically, the results indicate it is better to keep L:C ratio smaller than 2:3. This result is in general agreement with the modeling study of Lin and Nguyen [61] in which they have performed performance simulations with L:C ratios of 1:3, 1:1 and 3:1 and concluded that, cell performance increases with decreasing L:C ratio. Furthermore, they found that liquid saturation under the landings is always higher than that of under the channels, as confirmed in our tests. Our results are also in agreement with the numerical study of Yan et al. [62]. They investigated the effects of channel width fraction on the transport phenomena. In their model, channel width fraction, λ, was defined as the ratio of the channel width to landing width. The results showed that high λ values yield in more uniform oxygen and current distribution through the channel–DM interface. The cell performance also found to be improved as λ values increase from 0.25 to 1.

In summary, the residual water content in the fuel cell DM and channels strongly depends on channel size, landing size and L:C ratio. For smaller channel size, larger channel size or larger L:C ratio, the residual water in both the channels and the entire DM increases drastically. Furthermore, this configuration yields significant performance loss due to flooding behavior.

*3.1.2. Channel–DM Interface effect*

The interfacial contact between the channel wall and DM is important and has to be considered independently from the L:C ratio effect. We compared water mass values of two extreme cases, the 0.5 × 0.5 configuration with highest number of channel–DM interfaces (48) and 2.0 × 2.0 configuration with lowest (12), where L:C ratio is unity for both cases. The neutron images for both cases at 0.2, 0.8 and 1.2 A $cm^{-2}$ current density are shown in Fig. 12.

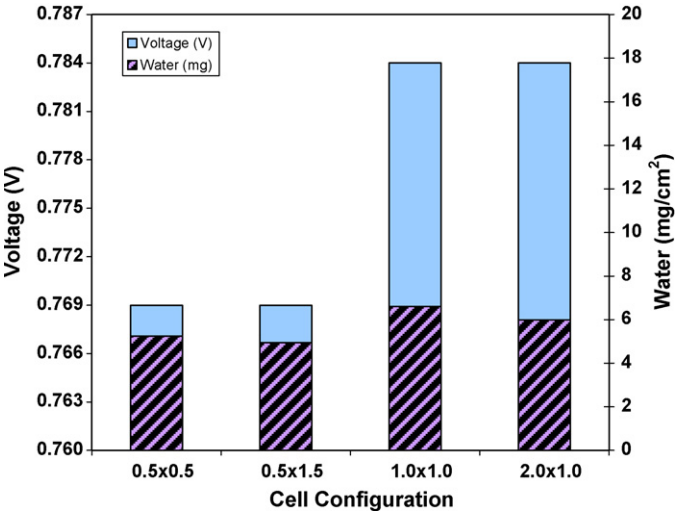


**Fig. 13.** Voltage and water mass values at 0.2 A $cm^{-2}$ and 50% RH conditions.

The 2.0 × 2.0 case has less water compared to 0.5 × 0.5 at each current density indicating the effect of channel–DM interface. In Pekula et al. [57], it is shown that for a serpentine flow field, switch backs tend to preferentially accumulate liquid water and a more linearized design is preferred to reduce water overhead. From the figure, it is also seen that there is favorable water accumulation at the 90° corners. Since a higher number of interfaces is directly proportional to switch backs for a serpentine flow field, the 0.5 × 0.5 has four times more turns than the 2.0 × 2.0 case, which result in more liquid storage in this configuration at each current density. In the neutron images, it is clear that most of the excess water at each current density is around the turns, and the remaining active area is similar between 0.5 × 0.5 and 2.0 × 2.0 cases which supports our explanation. Hence for a serpentine design, it is preferred to have a reduced number of interfaces (and u-turns) to reduce the water amount in the cell.

*3.2. Low humidity testing*

To simulate automotive operating conditions, 50% relative humidity input were compared with the fully humidified cases. In Fig. 13, voltage and water mass values at low current density (0.2 A $cm^{-2}$) and 50% RH are shown for various configurations.

Channel and landing width does not have a significant impact on performance and liquid water storage at this low current condition since both the voltage and water mass values are almost the same between 0.5 × 0.5 and 0.5 × 1.5 cases and between 1.0 × 1.0 and 2.0 × 1.0 cases. At higher L:C ratios, however, cell performance increases with increasing water content. For the fully humidified conditions, on the other hand, we showed that higher L:C ratio adversely effects the performance. This contradiction can be explained through membrane dehydration. At fully humidified conditions, the major limitation to the performance is flooding. At dry operation, however, membrane dehydration is the dominant mode of performance loss. Membrane conductivity is highly dependent on its water content, and at dry operation, inlet gases are generally insufficient to adequately hydrate the membrane. If the cell is operated at a low current, then there is not enough water generation in the catalyst layer to hydrate the membrane. Therefore, liquid water accumulation in the cell becomes necessary to supply additional

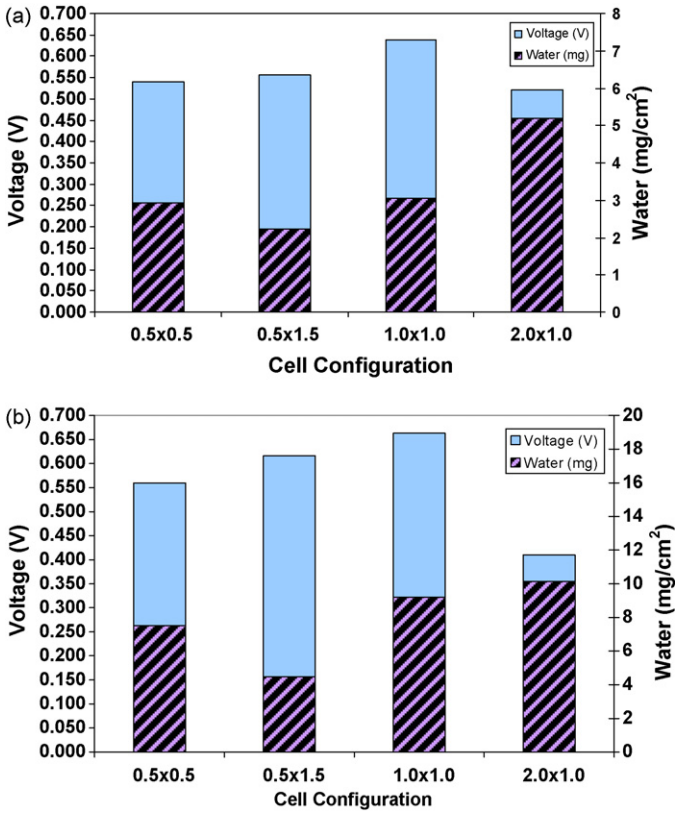


**Fig. 14.** Voltage and water mass values at (a) high current density (1.2 A cm$^{-2}$) and 50% RH, (b) 1.0 A cm$^{-2}$ and 100% RH conditions.

water to the membrane and obtain suitable proton conductivity. At high L:C ratio, less of the generated water is removed and the membrane can be hydrated better. Additionally, evaporative removal into the channel is restricted. As the current density increases, however, the water generated becomes adequate to hydrate the membrane. In this case, transport loss due to flooding overcomes the dehydration of the membrane and L:C ratio effect at dry operation becomes similar to that at fully humidified condition. In Fig. 14, results of high current operation for the same configurations are shown at 50 and 100% RH. The water accumulation compared to performance behavior is similar for both cases. As L:C gets larger, water storage increases and performance drop occurs. In summary, the large landing small channel design (large L:C ratio) provides better membrane hydration but poor gas transport due to high liquid water storage and therefore, it is best for low current, dry inlet gas operation in which membrane dehydration is the limiting factor on performance. On the other hand, the small landing large channel case (small L:C ratio) enables effective gas transport to the catalyst layer by reducing the liquid water amount in the channel and DM but does not support the necessary water to hydrate the membrane. Hence, this design is preferred for wet conditions and high current density operations.

## 4. Conclusions

In this study, extensive neutron imaging experiments were performed using seven different flow-field geometries with varying L:C ratios, and liquid water accumulation and residual water content in the fuel cell was analyzed at relatively dry and fully humidified inlet conditions. Results indicate: (1) for L:C ratios of one, the liquid water tends to preferentially accumulate under landings rather than under in, or under the channels, (2) water storage is not only a function of diffusion media but also dependent on the flow-field geometry and the number of interfaces for a hydrophilic channel wall, (3) it is possible to obtain similar cell performance at low to moderate current density with vastly different amounts of stored water by tailoring the flow-field geometry, (4) as the L:C ratio is reduced, the liquid stored in the cell decreases, with an optimal condition for L:C ratios smaller than 2:3, (5) the number of channel–DM interface for the same L:C ratio has an important influence on water accumulation. Corners are preferred water storage sites and a reduced number of channel–DM interface corresponds to less corners and turns for a serpentine design which results in low water mass in the cell, (6) at dry operation, a high L:C ratio can be helpful, while at high humidity ratio, a low L:C is preferred.

## Acknowledgements

The authors wish to thank General Motors Corporation for supporting this work and Dr. Tom Trabold and Dr. Po-Ya Abel Chuang for many useful discussions.

## Appendix A

Calculation of single-phase mass transfer of liquid water into the reactant flow:

$$D_h = \frac{4 \times A_c}{P} \tag{A.1}$$

where $D_h$ is the hydraulic diameter, $A_c$ is the flow cross-sectional area and $P$ is the wetted perimeter.

$$h_m = \frac{Sh_d D_{AB}}{D_h} \tag{A.2}$$

where $Sh_d$ is the Sherwood number, $D_{AB}$ is the diffusivity of molecule A in B

For steady, laminar, fully developed flow with uniform surface temperature, the Sherwood number is constant and given as

$$Sh_d = 3.08$$

The mass transfer rate of liquid water can be determined from

$$\dot{m} = h_m A_s(\rho_s - \rho_\infty) \tag{A3}$$

where $A_s$ is the surface area.

Cell configuration (L/C):

(a) $1.0 \times 0.75$

$$D_{h,a} = \frac{4 \times (0.75 \times 0.5)}{2 \times (0.75 + 0.5)} = 0.6$$

$$A_{s,a} = 0.75 \times 1 = 0.75$$

where channel length is taken as unity.

(b) $0.5 \times 1.5$

$$D_{h,b} = \frac{4 \times (1.5 \times 0.5)}{2 \times (1.5 + 0.5)} = 0.75$$

$$A_{s,b} = 1.5 \times 1 = 1.5$$

where channel length is taken as unity.

Calculating the mass transfer of liquid water as a ratio of configuration (a) to (b).

$$\frac{\dot{m}_a}{\dot{m}_b} = \frac{h_{m,a}A_{s,a}(\rho_{s,a} - \rho_\infty)}{h_{m,b}A_{s,b}(\rho_{s,b} - \rho_\infty)} \quad \text{(A4)}$$

where concentration terms cancels out since both cases have same operating conditions and reactant flow.

$$\frac{\dot{m}_a}{\dot{m}_b} = \left(\frac{(Sh_d D_{AB}/D_{h,a})}{(Sh_d D_{AB}/D_{h,b})}\right) \times \left(\frac{A_{s,a}}{A_{s,b}}\right)$$

$$\frac{\dot{m}_a}{\dot{m}_b} = \left(\frac{D_{h,b}}{D_{h,a}}\right) \times \left(\frac{A_{s,a}}{A_{s,b}}\right) = \left(\frac{0.75}{0.6}\right) \times \left(\frac{0.75}{1.5}\right)$$

$$\frac{\dot{m}_a}{\dot{m}_b} = 0.625$$

Hence

$$\dot{m}_b = 1.6\dot{m}_a$$

## References


[1] M.M. Mench, Fuel Cell Engines, John Wiley & Sons Inc., New York, NY, United States, 2008.
[2] W.Y. Hsu, T.D. Gierke, J. Membr. Sci. 13 (3) (1982) 307–326.
[3] G.J.M. Janssen, M.L.J. Overvelde, J. Power Sources 101 (2001) 117–125.
[4] A.Z. Weber, J. Newman, J. Electrochem. Soc. 150 (7) (2003) A1008–A1015.
[5] P. Choi, R. Datta, J. Electrochem. Soc. 150 (12) (2003) E601–E607.
[6] K.S. Chen, M.A. Hickner, D.R. Noble, Int. J. Energy Res. 29 (2005) 1113–1132.
[7] A. Golpaygan, N. Ashgriz, Int. J. Energy Res. 29 (2005) 1027–1040.
[8] U. Pasaogullari, C.Y. Wang, K.S. Chen, J. Electrochem. Soc. 152 (2005) A1574.
[9] A. Hakenjos, H. Muenter, U. Wittstad, C. Hebling, J. Power Sources 131 (2004) 213–216.
[10] C. Ziegler, H.M. Yu, J.O. Schumacher, J. Electrochem. Soc. 152 (2005) A1555.
[11] X. Zhu, P.C. Sui, N. Djilali, J. Power Sources (2007), doi:10.1016/j.jpowsour.2008.03.005.
[12] E. Birgersson, M. Noponen, M. Vynnycky, J. Electrochem. Soc. 152 (2005) A1021.
[13] J.H. Nam, M. Kaviany, Int. J. Heat Mass Transfer 46 (2003) 4595–4611.
[14] A.Z. Weber, J. Newman, J. Electrochem. Soc. 152 (4) (2005) A677–A688.
[15] P.C. Sui, S. Kumar, N. Djilali, J. Power Sources 180 (2008) 410–422.
[16] P. Berg, K. Promislow, J. St. Pierre, J. Stumper, B. Wetton, J. Electrochem. Soc. 151 (2004) A341–A353.
[17] N.P. Siegel, M.W. Ellis, D.J. Nelson, M.R. von Spakovsky, J. Power Sources 128 (2004) 173–184.
[18] M.M. Mench, Q.L. Dong, C.Y. Wang, J. Power Sources 124 (2003) 90–98.
[19] E. Antolini, R.R. Passos, E.A. Ticianelli, J. Appl. Electrochem. 32 (2002) 383–388.
[20] A. Hakenjos, H. Muenter, U. Wittstadt, C. Hebling, J. Power Sources 131 (2004) 213–216.
[21] P.A. Chuang, A. Turhan, A.K. Heller, J.S. Brenizer, T.A. Trabold, M.M. Mench, Proceedings of the Third International Conference on Fuel Cell Science, Engineering and Technology, Paper #74051, 2005.
[22] X. Zhu, P.C. Sui, N. Djilali, J. Power Sources 172 (1) (2007) 287–295.
[23] J.J. Baschuk, X. Li, J. Power Sources 86 (2000) 181–196.
[24] C. Lim, C.Y. Wang, Electrochim. Acta 49 (2004) 4149–4156.
[25] M.M. Mench, C.Y. Wang, J. Electrochem. Soc. 150 (1) (2003) A79–A85.
[26] J. Ihonen, M. Mikkola, G. Lindbergh, J. Electrochem. Soc. 151 (8) (2004) A1152–A1161.
[27] C.S. Kong, D.Y. Kim, H.K. Lee, Y.G. Shul, T.H. Lee, J. Power Sources 108 (2002) 185–191.
[28] L.R. Jordan, A.K. Shukla, T. Behrsing, N.R. Avery, B.C. Muddle, M. Forsyth, J. Power Sources 86 (2000) 250–254.
[29] E.C. Kumbur, K.V. Sharp, M.M. Mench, J. Electrochem. Soc. 154 (12) (2007) B1295–B1304.
[30] E.C. Kumbur, K.V. Sharp, M.M. Mench, J. Power Sources 168 (2) (2007) 356–368.
[31] M. Oszcipok, D. Riemann, U. Kronenwett, M. Kreideweis, M. Zedda, J. Power Sources 145 (2005) 407–415.
[32] J. Healy, C. Hayden, T. Xie, K. Olson, R. Waldo, M. Brundage, H. Gasteiger, J. Abbott, Fuel Cells 5 (2) (2005) 302–308.
[33] V.V. Nikam, R.G. Reddy, J. Power Sources 152 (2005) 146–155.
[34] M. Sundaresan, R.M. Moore, J. Power Sources 145 (2005) 534–545.
[35] E. Cho, J.J. Ko, H.Y. Ha, S.A. Hong, K.Y. Lee, T.W. Lim, I.H. Oh, J. Electrochem. Soc. 151 (5) (2004) A661–A665.
[36] E.C. Kumbur, K.V. Sharp, M.M. Mench, J. Power Sources 161 (1) (2006) 333–345.
[37] X. Li, I. Sabir, Int. J. Hydrogen Energy 30 (2005) 359–371.
[38] A.A. Kulikovsky, J. Divisek, A.A. Kornyshev, J. Electrochem. Soc. 146 (11) (1999) 3981–3991.
[39] E. Birgersson, M. Vynnyycky, J. Power Sources 153 (2006) 76–88.
[40] D.L. Wood, J.S. Yi, T.V. Nguyen, Electrochim. Acta 43 (24) (1998) 3795–3809.
[41] F. Chen, Y.Z. Wen, H.S. Chu, W.M. Yan, C.Y. Soong, J. Power Sources 128 (2004) 125–134.
[42] A. Kumar, R.G. Reddy, J. Power Sources 113 (2003) 11–18.
[43] S. Kim, S. Shimpalee, J.W. Van Zee, J. Electrochem. Soc. 152 (6) (2005) A1265–A1271.
[44] H.C. Liu, W.M. Yan, C.Y. Soong, F. Chen, H.S. Chu, J. Power Sources 158 (2006) 78–87.
[45] S.D. Knights, D.P. Wilkinson, US Patent No. 6,756,149 (2004).
[46] S. Shimpalee, S. Greenway, J.W. Van Zee, J. Power Sources 160 (2006) 398–406.
[47] X. Li, I. Sabir, J. Park, J. Power Sources 163 (2007) 933–942.
[48] W.M. Yan, H.C. Liu, C.Y. Soong, F. Chen, J. Power Sources 161 (2006) 907–919.
[49] W.M. Yan, C.H. Yang, C.Y. Soong, F. Chen, S.C. Mei, J. Power Sources 160 (2006) 284–292.
[50] F.B. Weng, A. Su, C.Y. Hsu, C.Y. Lee, J. Power Sources 157 (2006) 674–680.
[51] D. Kramer, E. Lehmann, G. Frei, P. Vontobel, A. Wokaun, G.G. Scherer, Nucl. Instrum. Methods Phys. Res. A 542 (2005) 52–60.
[52] D. Kramer, J. Zhang, R. Shimoi, E. Lehmann, A. Wokaun, K. Shinohara, G.G. Scherer, Electrochem. Acta 50 (2005) 2603–2614.
[53] J. Zhang, D. Kramer, R. Shimoi, Y. Ono, E. Lehmann, A. Wokaun, K. Shinohara, G.G. Scherer, Electrochem. Acta 51 (2006) 2715–2727.
[54] D.J. Ludlow, C.C. Calebrese, S.H. Yu, C.S. Dannehy, D.L. Jacobson, D.S. Hussey, M. Arif, G.A. Eisman, J. Power Sources 162 (2006) 271–278.
[55] Y.S. Chen, H. Peng, D.S. Hussey, D.L. Jacobson, D.T. Tran, T.A. Baset, M. Biernacki, J. Power Sources 170 (2007) 376–386.
[56] M.A. Hickner, N.P. Siegel, K.S. Chen, D.N. McBrayer, D.S. Hussey, D.L. Jacobson, M. Arif, J. Electrochem. Soc. 153 (5) (2006) A902–A908.
[57] N. Pekula, A. Heller, P.A. Chuang, A. Turhan, M.M. Mench, J.S. Brenizer, K. Unlu, Nucl. Instrum. Methods Phys. Res. A: Accel., Spectrometers, Detectors Assoc. Equip. 542 (1–3) (2005) 134–141.
[58] A. Turhan, K. Heller, J.S. Brenizer, M.M. Mench, J. Power Sources 160 (2006) 1195–1203.
[59] J.J. Kowal, A. Turhan, K. Heller, J.S. Brenizer, M.M. Mench, J. Electrochem. Soc. 153 (10) (2006) A1971–A1978.
[60] T.A. Trabold, J.P. Owejan, D.L. Jacobson, M. Arif, P.R. Huffman, Int. J. Heat Mass Transfer 49 (2006) 4712–4720.
[61] G. Lin, T.V. Nguyen, J. Electrochem. Soc. 153 (2) (2006) A372–A382.
[62] W.M. Yan, C.Y. Soong, F. Chen, H.S. Chu, J. Power Sources 125 (2004) 27–39.